IJMSA
International Journal of Microgravity Science and Application
JASMA
Original Paper

# Elimination of Systematic Error in Diffusion Measurement Using In-situ X-ray Fluorescence Analysis for Liquid Alloys

**Yoshihiro KOBAYASHI[1*], Masato SHIINOKI[2,3], Seiya KATO[4], Tadahiko MASAKI[5], Shinsuke SUZUKI[1,2,4]**

[1] Department of Materials Science, Waseda University, Tokyo Japan
[2] Kagami Memorial Institute of Materials Science and Technology, Waseda University, Tokyo Japan
[3] Institute of Materials Physics in Space, German Aerospace Center, Cologne Germany
[4] Department of Applied Mechanics and Aerospace Engineering, Waseda University, Tokyo Japan
[5] Department of Materials Science and Engineering, Shibaura Institute of Technology, Tokyo Japan
* Correspondence: yuugen-wabi@asagi.waseda.jp

**Abstract:** The objective of the present study is to quantify and eliminate the error factors in the measurement of diffusion coefficients in liquid alloys by using in-situ X-ray fluorescence analysis (in-situ XRF). Averaging effect, initial mass transport, and matrix effect were investigated. The impurity diffusion coefficient of Bi in liquid Sn was measured at 573 K using a combination of the long capillary technique and in-situ XRF. The apparent diffusion coefficient was obtained as the time-series data by fitting an analytical solution of Fick's second law to the temporal variation in Bi concentration in the capillary. In the present measurement, matrix effect did not induce a significant error in the measured diffusion coefficient. Averaging effect can be eliminated by convoluting the analytical solution with the distribution of the X-ray fluorescence intensity scanned from the rod sample. Furthermore, the initial mass transport can be eliminated by shifting the point of time origin to the latter time in the temporal variation in the measured concentration by fitting the analytical solution. By performing the above corrections, the systematic error in the measured diffusion coefficient can be reduced.

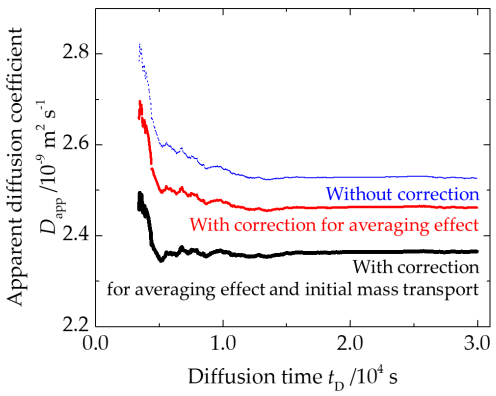


**Keywords:** Diffusion, Liquid alloys, X-ray fluorescence analysis, In-situ measurement, Long capillary technique
**Article History:** Received 24 April 2023, accepted 20 September 2023, published 31 October 2023.

## 1. Introduction

The diffusion phenomena in liquid metals are important to understand the solidification of metallic materials and their dynamics in liquid metals. Accurate data for diffusion coefficients in liquid metals are required to elucidate the diffusion phenomena and advance the above research fields. To enhance the accuracy of the measured diffusion coefficient, the dominant error factors in diffusion measurements should be quantified and eliminated. Conventionally, natural convection has caused systematic errors in the measured diffusion coefficient[1,2]. Several measurement techniques have been proposed to eliminate natural convection, such as measurements under microgravity conditions, adopting stable density laying, and measurements in a static magnetic field[3-8]. However, the concentration analysis of the sample also causes systematic error, particularly for liquid metals.

Several concentration analysis techniques for diffusion measurements of liquid metals are summarized in **Table 1**. The diffusion coefficient is conventionally calculated from the concentration distribution of a diffusion couple in a capillary using the long capillary (LC) technique. Conventionally, ex-situ concentration analysis has been applied to cooled solidified samples for diffusion measurements. For the ex-situ analysis of LC, the measured mass transport is altered by several error factors induced during heating and cooling, such as a disturbance at an initial state, diffusion when the temperature is not intended, and segregation and shrinkage of the sample. The shear cell (SC) technique eliminates the error factors by shearing the capillary into several cells during heating and cooling[9-12]. However, SC induces shear convection. It is an additional mass transport caused by shearing of the capillary[13].

Recently, in-situ concentration analyses were adopted for diffusion measurements to determine their concentrations in liquid metals. The error factors during heating and cooling can be eliminated by analyzing the concentration distribution in the melted sample. In-situ X-ray radiography (in-situ XRR) has been adopted for LC or SC to eliminate additional mass transport and analyze the dependence of the concentration or temperature on the diffusion[14-17]. However, the materials measured for in-situ XRR are limited to binary alloys, where the contrast between the components in the radiographic image is significant.

In-situ X-ray fluorescence analysis (in-situ XRF) can also be applied to diffusion measurements in multi-component alloys[18-20]. Using a combination of LC and in-situ XRF, the apparent diffusion coefficient can be obtained as time-series data from the temporal variation in the concentration at a fixed point in the capillary. Our previous research reported that the apparent diffusion coefficient converges by increasing the diffusion time but is overestimated. This is particularly so for a short diffusion time[21]. To enhance the accuracy of the diffusion measurements, the dominant error factors that induce the overestimation of the apparent diffusion coefficient should be eliminated. However, systematic errors in diffusion measurements owing to several error factors have not been quantified in previous research.

The objective of the present study is to quantify and eliminate the error factors that induce the overestimation of the apparent diffusion coefficient obtained by in-situ XRF and LC. In this study, several error factors were investigated, including averaging effect, initial mass transport, and matrix effect, as described in Section 2. To quantify the systematic errors in the measured diffusion coefficient, the impurity diffusion coefficient of Bi in liquid Sn was measured at 573 K using in-situ XRF and LC. The validity of measured values can be evaluated conveniently using previously measured values[8,13,22].

**Table 1.** Characteristics of concentration analysis techniques for diffusion measurements in liquid metals.

| Concentration analysis | Error factor for measured mass transport | Available sample material | Available container material |
|---|---|---|---|
| Ex-situ | · Initial mass transport<br>· Diffusion during heating-up and cooling-down<br>· Segregation<br>· Shrinkage | · Materials with low reactivity with container | · No limitation |
| In-situ XRR[*1] | · Initial mass transport | · Binary alloys with significant contrast in a radiographic image | · Materials with high X-ray transmissibility |
| In-situ XRF[*2] | · **Averaging effect**<br>· **Initial mass transport** | · Materials where **matrix effect** does not occur significantly | · Materials with high X-ray transmissibility |

[*1]XRR: X-ray radiography, [*2]XRF: X-ray fluorescence analysis, **Bold**: Investigated error factors in this study.

## 2. Proposed error factors

The features and sources of the three proposed error factors are summarized in **Fig. 1**. Averaging effect is the overestimation of the measured diffusion coefficient caused by smoothing of the concentration distribution in a diffusion couple. The initial mass transport is the disturbance in the initial state of the diffusion measurement. Matrix effect is the absorption or enhancement of the X-ray fluorescence of a solute element caused by a solvent element in the alloys. The following sections explain this phenomenon in detail.

| Error factor | Source | Schematics |
|---|---|---|
| Averaging effect | Existence of X-ray irradiation range in a capillary | (a) X-ray irradiation range 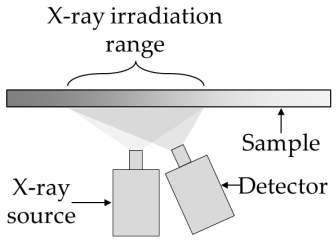  |
| Initial mass transport | Additional mass transport induced at the initial state | (b) Diffusion couple at the initial state 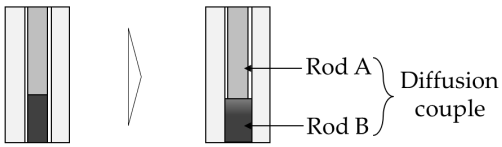  |
| Matrix effect | Absorption or enhancement effect on the X-ray fluorescence | (c) Matrix effect in liquid alloys 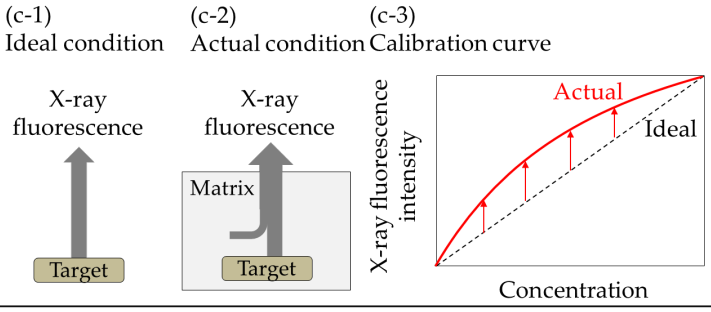  |

**Figure 1.** Sources and schematics of proposed error factors in diffusion measurements using in-situ XRF and LC. (a) X-ray irradiation range. (b) Diffusion couple at the initial state. (c) Matrix effect in liquid alloys.

## 2.1. Averaging effect

For in-situ XRF and LC, the concentration is measured as the actual value convoluted with the distribution of the scanned X-ray fluorescence intensity, as shown in **Fig. 2**. The measured concentration can be expressed as

$$c_2(x, t) = \int_{-\infty}^{\infty} c_1(u, t)\rho_I(x\text{-}u)\mathrm{d}u, \tag{1}$$

where $c_1(u, t)$ is the analytical solution of Fick's second law with a position $u$ and time $t$, $\rho_I(x\text{-}u)$ is the intensity scanned from a position $u$ in the capillary, and $x$ is the position of the center of the X-ray irradiated range. Averaging effect is eliminated by fitting $c_2(x, t)$ to the measured concentration distribution[20]. In the above analysis, the $\rho_I(x\text{-}u)$ function should be prepared according to an experimental apparatus.

## 2.2. Initial mass transport

If the melting points of the rods in a diffusion couple are significantly different, one rod with a higher melting point would be dissolved, although another rod remains solid during heating. The concentration

distribution in the initial state would be disturbed owing to the above dissolution. Thus, the measured mass transport would be overestimated. In-situ measurements are effective for identifying the amount of overestimated mass transport by monitoring the variation in concentration in the diffusion couple. For in-situ XRF, the overestimated mass transport should be quantified by shifting the time origin point to a latter time in the temporal variation in the measured concentration.

### 2.3. Matrix effect

Matrix effect induces nonlinearity in the calibration curve of the X-ray fluorescence intensity and concentration[23,24]. In experiments using XRF, matrix effect should be corrected to improve the accuracy of the concentration analysis[25-29]. A systematic error in the measured concentration deteriorates the accuracy of the measured diffusion coefficient. Sn atoms enhance the X-ray fluorescence of Bi in liquid Sn-Bi alloys[30]. The significance of the systematic error in the measured diffusion coefficient owing to the above enhancement should be investigated in the measurement for the impurity diffusion, where the maximum Bi concentration is approximately 10 atomic percentage (at.%).

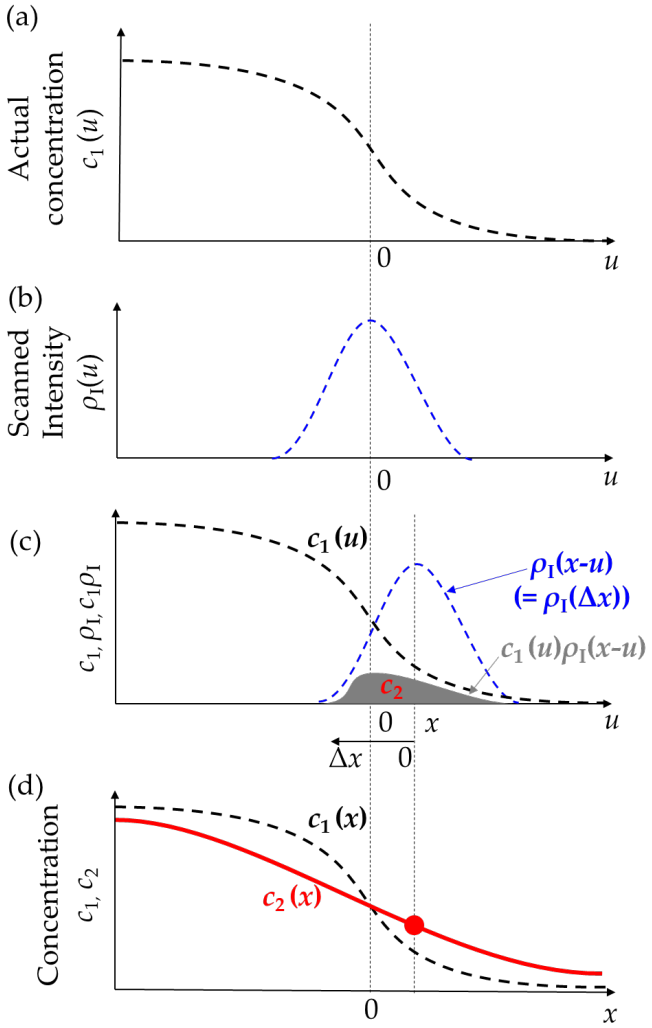


**Figure 2.** Schematics of a cause of averaging effect. The symbols $u$ and $x$ are the position in a capillary and position of the center of the X-ray irradiated range, respectively. (a) Actual concentration in a capillary. It can be expressed as the analytical solution $c_1(u, t)$. (b) Distribution $\rho_I(x\text{-}u)$ of the scanned intensity in the capillary. (c) Schematics of the convolution. Black line: $c_1(u, t)$, Blue line: $\rho_I(x\text{-}u)$, Gray area: Integral value of $c_1(u, t)\rho_I(x\text{-}u)$. (d) Actual concentration $c_1(x, t)$ and measured concentration $c_2(x, t)$ in the capillary.

## 3. Experimental procedure

The experimental apparatus was identical to that used in previous studies[21,31], as shown in **Figs. 3** and **4(a)**. To evaluate averaging and matrix effect in the diffusion measurement, the distribution of the X-ray fluorescence intensity detected from a point in the capillary and the calibration curve between the X-ray fluorescence intensity and concentration were prepared in Subsections 3.1 and 3.2, respectively. Diffusion measurements were performed using two types of diffusion couples under different concentration conditions, as described in Subsection 3.3. To quantify the initial mass transport in the diffusion measurement, the diffusion couple was melted partially, as described in Subsection 3.4.

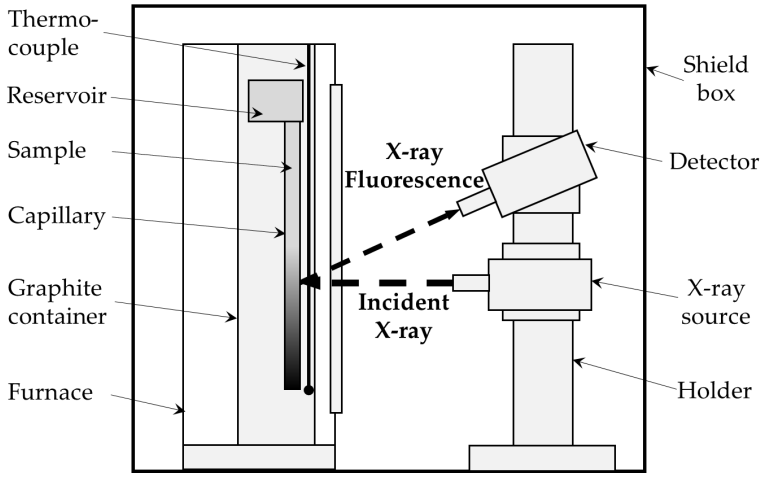


**Figure 3.** Schematics of the experimental apparatus. The apparatus was identical that in a previous study[21].

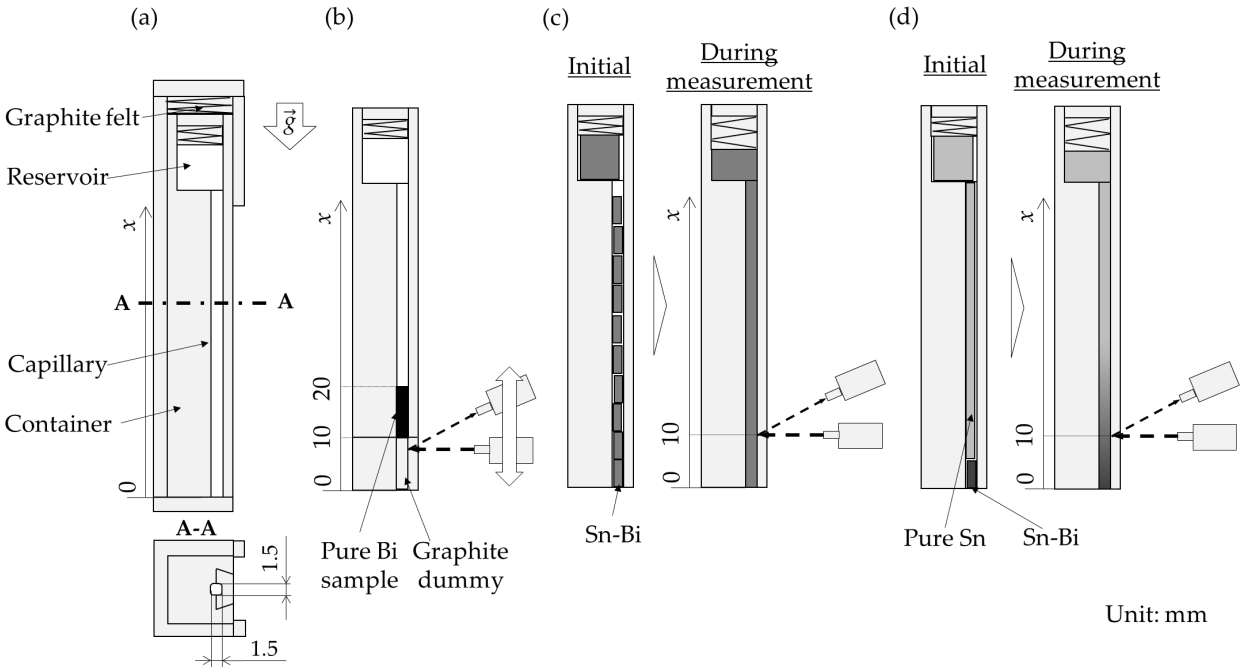


**Figure 4.** Schematics of the sample placement in the experiment; (a) Overview of the capillary. The vector $\vec{g}$ shows the direction of gravity. (b-d) The setup and measurement state of each experiment; (b) Measurement for distribution of detected intensity. (c) Preparation for the calibration curve. (d) Diffusion measurement and measurement for boundary shape of diffusion couple.

### 3.1. Measurement for distribution of detected intensity

A pure Bi sample rod and graphite dummy rod were placed in the capillary, as shown in **Fig. 4(b)**. The size of the capillary was 1.5 mm × 1.5 mm × 63 mm with fillets of 0.3 mm. The Bi rods were prepared from pure Bi grains (99.999 mass%, Kojundo Chemical Laboratory Co., Ltd.). The grains were melted and cast at 873 K into a square rod of 1.5 mm × 1.5 mm × 10 mm with fillets of 0.3 mm. The graphite rod of 1.5 mm × 1.5 mm × 10 mm with fillets of 0.3 mm was set at the bottom of the capillary. The cast sample rod was set on the graphite rod. A pure Sn sample was prepared to quantify the background intensity of the X-ray fluorescence of Bi. The casting process and settings for the pure Sn sample were the same as those of the pure Bi sample.

The X-ray fluorescence was detected from the sample rod at several measurement points in the capillary at room temperature. The capillary was set inside the furnace, and the pressure was maintained at less than 10 Pa using a rotary pump during the measurement. For the XRF apparatus, Mini-X2 and X123-SDD (Amptek, Inc.) were adopted as the X-ray source and detector, respectively. The samples were irradiated with X-rays 30 mm from the inner wall of the capillary. The output of the X-ray source was set to be 4.0 W with a current of 80 μA and voltage of 50 kV. A Cu film with a thickness of 25.4 μm was attached to the tip of the X-ray source as the X-ray filter[32]. The setting position of the center of the irradiated X-ray range was varied in the range between x = 6.5 mm and $x$ = 14.5 mm with steps of 0.1 mm. The $x$ position was defined as the distance from the bottom of the capillary, as shown in **Fig. 4**. X-ray fluorescence was detected in the sample with an integration time of 60 s and 4096 channels. The energy resolution of the detector was set as 7.66 eV per channel. This was approximated from the channel of the detected K$\alpha$ emission line of Fe (836th channel corresponding to 6.40 keV[33]). The detected intensity of the L$\alpha$ emission line of Bi (Bi L$\alpha$ intensity) was calculated as the sum of the detected intensities in the peak range from the 1385th to 1435th channels (corresponding to from 10.60 to 10.99 keV, containing the center of the Bi L$\alpha$ peak at 10.83 keV[33]). The intensity, $I$, detected for pure Bi was subtracted from the background intensity, which was defined as the intensity detected for pure Sn.

### 3.2. Preparation for a calibration curve

Bi L$\alpha$ intensities were detected from several Sn-Bi rods with Bi concentrations of 0, 0.5, 1.0, 1.5, and 2.0 at.%, as shown in **Fig. 4(c)**. Pure Sn and Bi were weighed and mixed to form the Sn-Bi alloys. Ten pieces of 1.45 mm ×1.45 mm ×6 mm each with fillets of 0.3 mm were fabricated by casting each Sn-Bi alloy. One of the pieces with a size of ϕ4.5 mm × 5 mm$^3$ was also fabricated by casting this Sn-Bi alloy. Each pair of 10 square rods and a cylindrical mold were contained in the capillary and reservoir, respectively.

The temperature of the capillary was maintained at 573 K for 6000 s to melt the Sn-Bi rods. It was controlled using a proportional-integral-differential control device, YTC-3030 (Yonekura Mfg. Co., Ltd.). The capillary was filled with a Sn-Bi alloy by providing the alloys from the reservoir during melting. The detailed setup of the XRF is identical to that described in Subsection 3.1. The center of the irradiated X-ray range was fixed at $x$ = 10 mm. The X-ray fluorescence of the melted sample was detected 100 times with an integration time of 60 s. The detected intensity with an integration time of 6000 s was calculated as the sum of 100 intensities with an integration time of 60 s for each measurement. The measurements were performed four times for each alloy. The Bi L$\alpha$ intensities $I$ were calculated as the sum of the detected intensities in the peak range, including the background. The background intensity was defined as the mean of the four intensities detected for pure Sn. A calibration curve was estimated as a linear function of the detected intensity $I$ at each Bi concentration $c_{Bi}$ using the least-squares method.

### 3.3. In-situ impurity diffusion measurement

The impurity diffusion of Bi in liquid Sn was observed using a diffusion couple of pure Sn rods and Sn-Bi rods, as shown in **Fig. 4(d)**. The lengths of the pure Sn and Sn-Bi rods were 60 and 3 mm, respectively. The Bi concentration of the Sn-Bi rod was set to 5 or 10 at.%. The Sn-Bi alloy was cast into a square rod of 1.45 mm × 1.45 mm with fillets of 0.3 mm. Its size was set to 1.5 mm × 1.5 mm × 3.0 mm with fillets of 0.3 mm at 573 K considering the thermal expansion. The pure Sn was cast into a square rod of 1.45 mm × 1.45 mm × 60 mm with fillets of 0.3 mm and a cylindrical mold of ϕ4.5 mm × 5 mm. The Sn-Bi rod was placed at the bottom of the capillary. A pure Sn rod was placed on the Sn-Bi rod to provide a stable density layer[4]. Each pair of square rods and the cylindrical mold were contained in the capillary and reservoir, respectively.

The container temperature was maintained at 573 K for 30000 s. The detailed setup of the measurement was identical to that described in Subsections 3.1 and 3.2. The point of time origin ($t$ = 0) in the diffusion

measurement was set as the time point when the temperature of the capillary attained the melting point of Sn, 505 K[34]. The X-ray fluorescence of the melted sample was detected continuously with an integration time of 60 s. The Bi concentration $c_{Bi}$ at each time was calculated from the detected Bi L$\alpha$ intensity $I$ by subtracting the background intensity and dividing by the gradient of the calibration curve. This was according to the calibration curve provided in Subsection 3.2.

### 3.4. Measurement for boundary shape of the diffusion couple

To observe the boundary shape of the diffusion couple in the initial state during the impurity diffusion measurement, an experiment was performed to melt the diffusion couple partially. The diffusion couple was prepared as described in Subsection 3.3. The initial Bi concentration in the Sn-Bi rods was set to 10 at.%. The capillary was heated to 503 K. This was higher than the liquidus temperature of Sn90Bi10 (approximately 480 K[34]) and lower than the melting point of Sn (505 K). The shape of the diffusion couple was observed after solidification and compared with that of the as-cast sample.

## 4. Results

### 4.1. Distribution of the detected X-ray intensity in the capillary

**Figure 5** shows the detected Bi L$\alpha$ intensities at several points in the measurement of pure Bi and graphite dummy, as described in Subsection 3.1. The detected intensity increased, and then remained almost constant when the irradiated point shifted upward. The Bi L$\alpha$ intensity increased before the irradiated point reached the boundary between the pure Bi and dummy. This indicated that the X-rays irradiated a certain range in the capillary rather than at a point. The distribution of the detected intensity was symmetric with the boundary between the sample and dummy and appeared to have the shape of the error function. The distribution of the detected intensity is equivalent to the cumulative distribution function of the intensity scanned by the capillaries. Therefore, the distribution of the scanned intensity can be approximated as a Gaussian function, whose cumulative distribution function can be expressed as an error function.

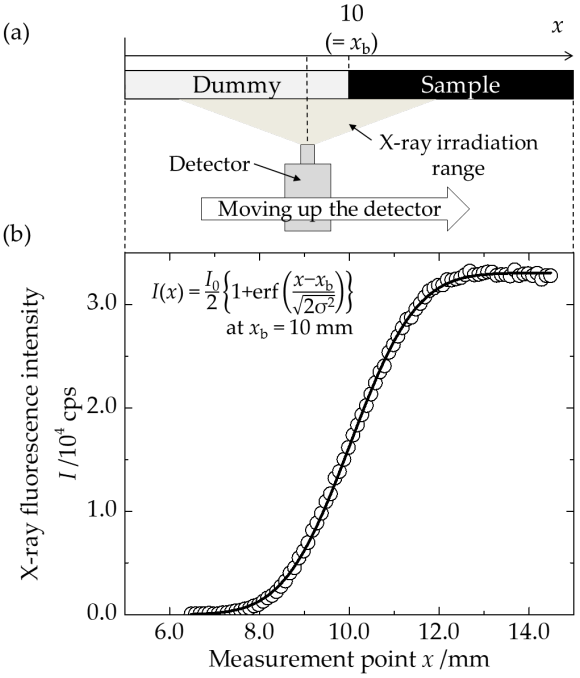


**Figure 5.** X-ray fluorescence intensity detected from a couple of the graphite and the pure Bi rod: (a) Schematics of the measurement; the $x$ position of irradiated X-ray range was varied around the boundary between the sample and dummy with a step of 0.1 mm. (b) Result of the measurement. Blank plot: Detected intensity. Black line: The error function (Eq. (3)) fitted to the detected intensities with value of the variables $I_0$ and $\sigma$.

## 4.2. Calibration curve

**Figure 6(a)** shows the X-ray fluorescence spectra obtained from the Sn-Bi rods for preparing the calibration curve, as described in Subsection 3.2. The detected intensity of the Bi L$\alpha$ peak increased with the Bi concentration. The peak around 11.5 keV corresponds to the Au L$\beta$ peak[32]. It was emitted from the gold plating in the furnace. **Figure 6(b)** shows the Bi L$\alpha$ intensities detected from all the Sn-Bi rods, including the pure Sn rod. Four plots were obtained for each Sn-Bi rod. The background intensity was calculated to be 4.2 cps, as described in Subsection 3.2. The detected intensity can be approximated as a linear function of the Bi concentration. **Figure 6(b)** shows the fitted linear function for all the plots as a red line. The gradient of the calibration curve was calculated as 14.8 cps/at.%. Each standard deviation of four intensities detected from the same rod was less than 0.40 cps. This was equivalent to 0.02 at.% in the calibration curve. The lower limit of quantitation was 0.18 at.%. This was estimated to be ten-times the statistical error in counting by the detector. The statistical error was calculated as the square root of background intensity[23].

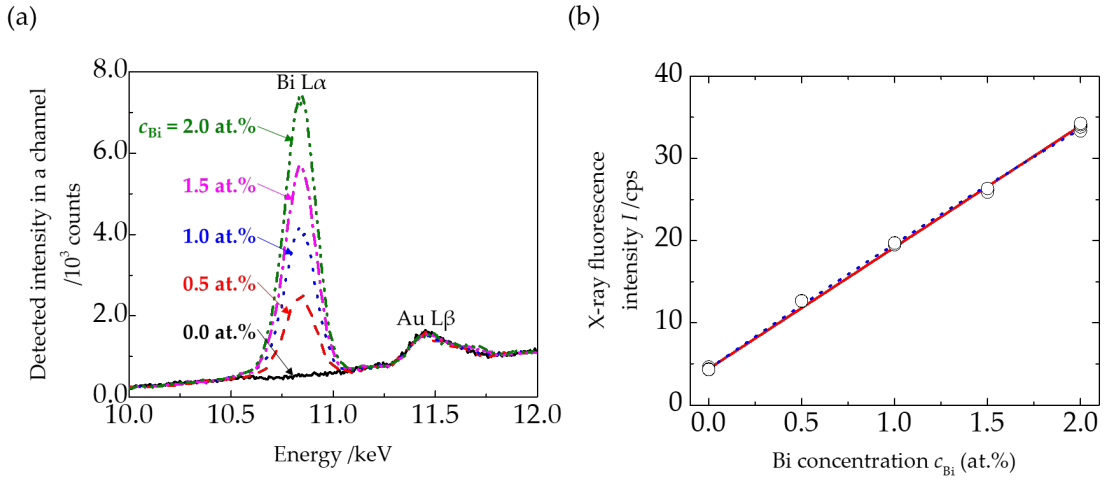


**Figure 6.** Results of the experiments for a calibration curve. (a) Examples of X-ray fluorescence spectra obtained from the Sn-Bi rods with Bi concentrations $c_{Bi}$ of 0, 0.5, 1.0, 1.5, and 2.0 at.%. (b) Detected Bi L$\alpha$ intensity (intensity in the peak range) at each Bi concentration. The intensity was detected four times from each Sn-Bi rod and is illustrated as four plots at each concentration. Blank plot: Detected intensity in the experiment. Solid red line: A fitted linear function. Dotted blue line: A fitted quadratic function.

## 4.3. Variation in the Bi concentration in the diffusion measurement

**Figure 7** shows the Bi concentrations measured in the diffusion measurements, as described in Subsection 3.3. The temperature of the container converged to 573 K over the range of ±0.1 K until $t$ = 197 s in both the diffusion measurements. The concentration exceeded the lower limit of quantitation after $t$ = 3159 and 2242 s when the initial Bi concentration was 5 and 10 at.%, respectively. The Bi concentration initially increased and then decreased marginally. The trends of variation in the Bi concentration in both the measurements were similar as observed.

## 4.4. Boundary shape of the diffusion couple at initial states

**Figure 8(a)** shows the shape of the diffusion couple after partial melting and solidification. Before melting, the shape of the as-cast Sn-Bi rod was smaller than that of the crucible. The length of the as-cast Sn-Bi rod was measured to be 3.46 mm using a vernier caliper. After partial melting and solidification, the pure Sn and Sn-Bi rods remained separated. This indicates that pure Sn did not dissolve in the partially melted Sn-Bi rod. The length of the solidified Sn-Bi rod was measured to be 3.48 mm. The top of the Sn-Bi rod was rounded, and the length at the edge of the rod was shorter than that at its center. The Sn-Bi rods were longer than the planned lengths for both as-cast and post-partial melting.

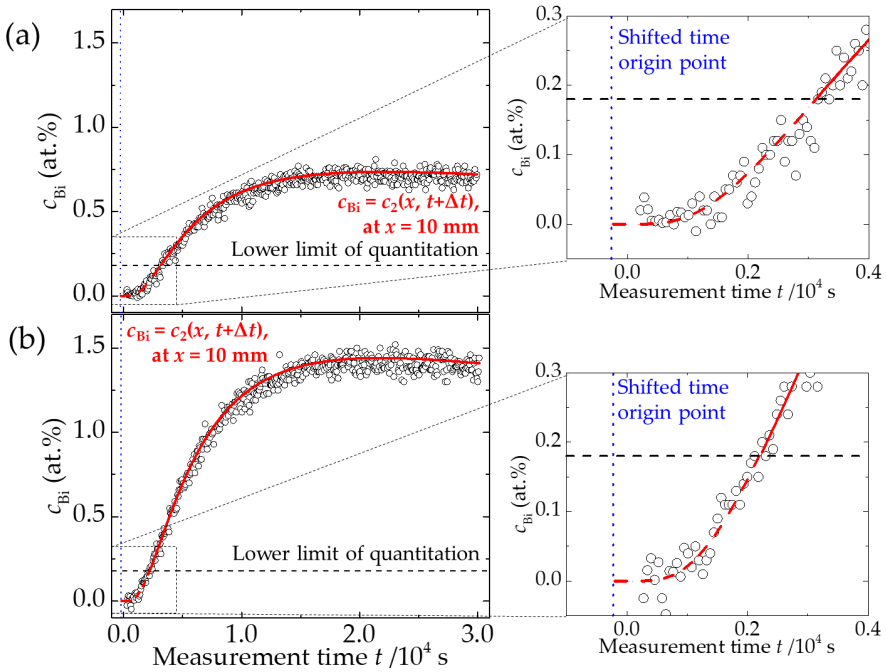


**Figure 7.** Measured concentrations in two diffusion measurements using the Sn-Bi rod with the Bi concentrations of (a) 5 at.% and (b) 10 at.%. Blank plot: Measured concentration. Solid red line: The analytical solution, $c_{Bi} = c_2(x, t+\Delta t)$, fitted to the measured concentration which was higher than the lower limit of quantitation of in-situ XRF. The $\Delta t$ values were obtained as (a) 265 s and (b) 230 s as variable values by fitting. Dashed red line: Extrapolation line of the fitted analytical solution. Dashed black line: The lower limit of quantitation, 0.18 at.% of Bi. Dotted blue line: Shifted time origin point.

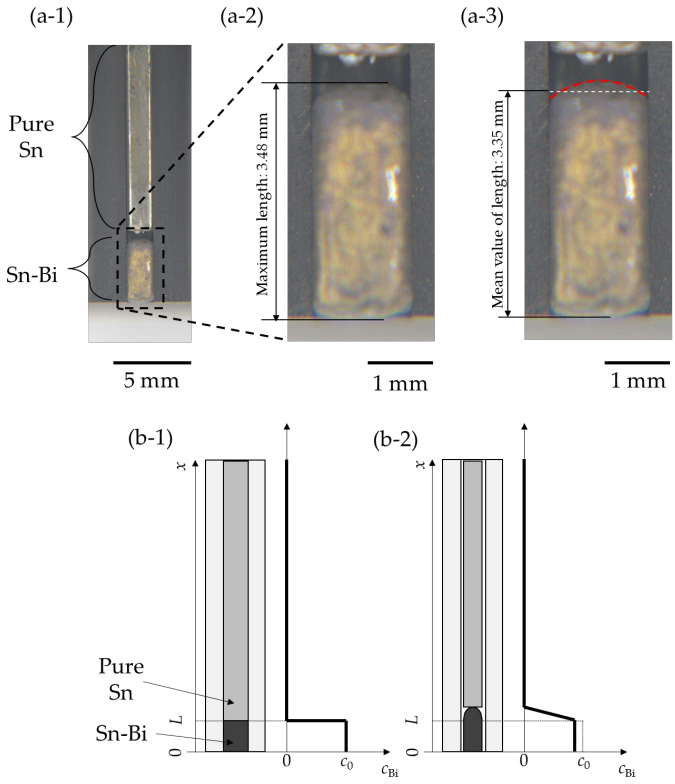


**Figure 8**. Boundary shape of diffusion couple after partial melting and solidification. (a) Photographs of the diffusion couples. Red dotted line: Quadratic function fitted to the shape of the Sn-Bi rod. White dotted line: The length obtained by averaging the volume of the shape expressed as the fitted quadratic function. (b) Schematics of the boundary shape of the diffusion couple at the initial state; (b-1) Planned and (b-2) actual.

## 5. Discussion

Averaging effect, initial mass transport, and matrix effect were quantified using the results of the diffusion measurements presented in Subsections 5.1, 5.2, and 5.3, respectively. After eliminating the error factors, the validity of the apparent diffusion coefficient is discussed in Subsection 5.4.

The apparent diffusion coefficient at a certain diffusion time was calculated by fitting the temporal variation in the concentration in the time range corresponding to the diffusion time to the analytical solution of Fick's second law. The details of this analysis were described in a previous study[21]. The concentration in the diffusion couple can be expressed as an analytical solution of Fick's second law as follows;

$$c_1(x, t) = \frac{c_0}{2}\left\{\mathrm{erf}\left(\frac{L+x}{\sqrt{4Dt}}\right)+\mathrm{erf}\left(\frac{L-x}{\sqrt{4Dt}}\right)\right\}, \tag{2}$$

where $c_0$ and $L$ are the Bi concentration and the length of the Sn-Bi rod in the initial state, respectively, and $D$ is the impurity diffusion coefficient of Bi in Sn. By fitting the analytical solution to the measured concentration variation, the apparent diffusion coefficient $D_{app}$ was obtained as a variable $D$ value.

### 5.1. Correction for averaging effect

In this study, the averaging effect was corrected by convoluting the analytical solution with the distribution of the scanned intensity in the capillary, as described in Eq. (1). The distribution of the scanned intensity was obtained from the distribution of the detected intensity from the capillary, as described in Subsection 4.1. By approximating the distribution of the scanned intensity as a Gaussian function, the distribution of the detected intensity can be expressed as

$$I(x) = \frac{I_0}{2}\left\{1+\mathrm{erf}\left(\frac{x-x_b}{\sqrt{2\sigma^2}}\right)\right\}, \tag{3}$$

where $I_0$ is total detected intensities in the capillary; $\sigma$ is the standard deviation of the Gaussian function in a width direction; and $x_b$ is the position of the boundary between the graphite and Bi rod, which was set as 10 mm in the experiment. The distribution of the detected intensity was fitted using Eq. (3) with the variables $I_0$ and $\sigma$, as described in **Fig. 5**. The fitness of Eq. (3) was evaluated based on the R-square value, which was calculated by subtracting one from the residual error. The R-square value was calculated to be higher than 0.999, indicating a good fit of Eq. (3). The $\sigma$ value of the fitted Eq. (3) was calculated to be 0.91 mm.

To obtain the apparent diffusion coefficient, the expected concentration variation in the capillary was calculated, and the systematic error in the apparent diffusion coefficient caused by averaging effect was quantified. The expected concentration was calculated as $c_{Bi} = c_2(x, t)$ using Eq. (1) in 0 s ≤ $t$ ≤ 30000 s with a time step of 60 s. The parameters in the $c_2(x, t)$ function were set identical to the experimental conditions, except for $D$ and the $\rho_I(\Delta x)$ function. The symbol $\Delta x$ corresponds to the distance from the center of the irradiation range to the detected point. In the calculation, the value of $x$-$u$ was substituted for $\Delta x$. The diffusion coefficient $D$ was set as $2.4 \times 10^{-9}$ m$^2$/s. This was the previously measured value in a reference[8]. The $\rho_I(\Delta x)$ function was defined as the Gaussian function:

$$\rho_I(\Delta x) = \frac{1}{\sqrt{2\pi\sigma^2}}\exp\left\{-\frac{(\Delta x)^2}{2\sigma^2}\right\}. \tag{4}$$

Here $\sigma$ was set as that of the fitted Eq. (3) in **Fig. 5**. **Figure 9(a)** shows the expected concentration variation calculated using the analytical solution $c_{Bi} = c_1(x, t)$ and corrected analytical solution $c_{Bi} = c_2(x, t)$. The expected concentrations obtained using these two functions were similar. However, in the initial state, the concentration increased owing to averaging effect.

The apparent diffusion coefficients were obtained from the expected concentrations by fitting the functions, $c_{Bi} = c_1(x, t)$ and $c_{Bi} = c_2(x, t)$. In the fitting, only concentrations higher than the lower limit of the quantitation were fitted. Therefore, $D_{app}$ could be calculated for $t_D$ > 3090 s. **Figure 9(b)** shows the apparent diffusion coefficients obtained from the expected concentration. When fitting $c_{Bi} = c_1(x, t)$, $D_{app}$ was initially overestimated and converged to a value that was 2.7% larger than the set value. When fitting $c_{Bi} = c_2(x, t)$, a few of the $D_{app}$ values did not differ significantly from the set values. This indicated that the apparent diffusion coefficient was overestimated by averaging effect. The systematic error owing to averaging effect was estimated to be 2.7% under the present experimental conditions.

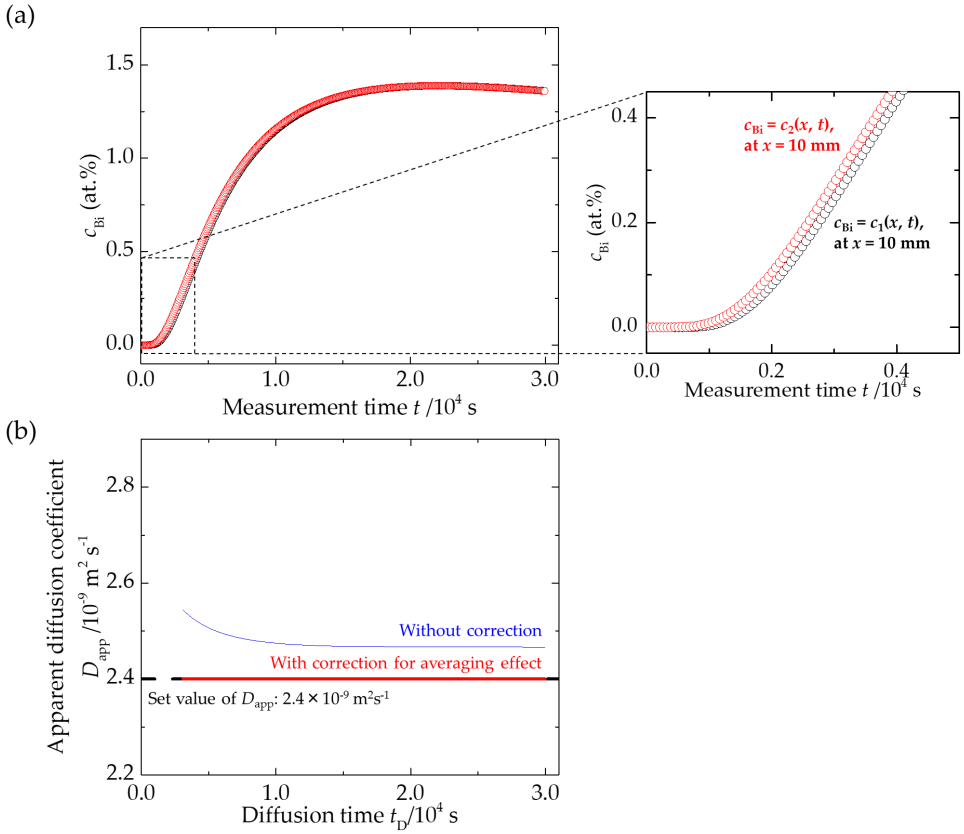


**Figure 9.** Apparent diffusion coefficients calculated from simulation results. (a) Analytical solution $c_{Bi} = c_1(x, t)$ and corrected analytical solution $c_{Bi} = c_2(x, t)$. (b) Apparent diffusion coefficients calculated from the expected concentration. Thin blue line: Without the correction for averaging effect. Thick red line: With the correction for averaging effect.

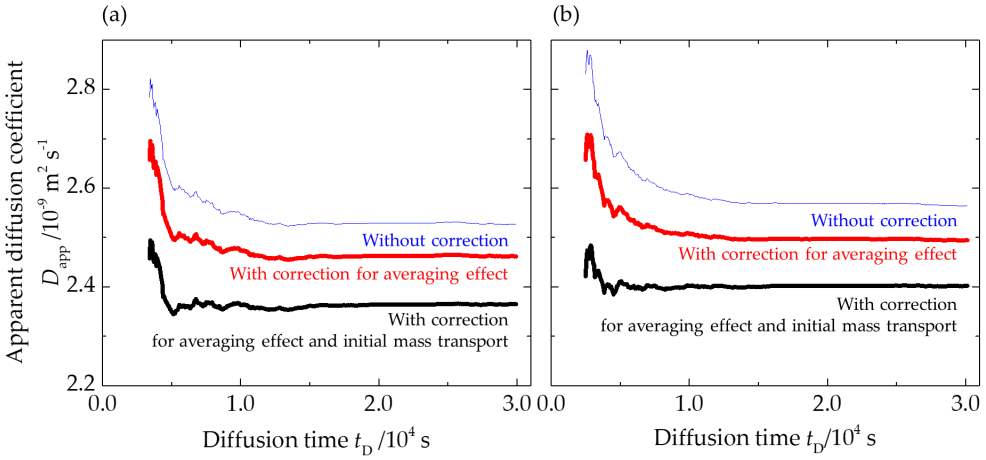


**Figure 10.** Apparent diffusion coefficients calculated from experimental results. The initial Bi concentrations of the Sn-Bi rod in the experiments were (a) 5 at.% and (b) 10 at.%. Thin blue line: Without the correction. Thick red line: With the correction for only averaging effect. Thick black line: With the correction for averaging effect and initial mass transport.

In the analysis of the experimental results, the apparent diffusion coefficient was obtained from the concentrations measured in the diffusion measurements. The calculation processes were identical to those used for the expected concentrations. **Figure 10** shows the apparent diffusion coefficients calculated from the measured concentrations. When fitting to $c_{Bi} = c_2(x, t)$, $D_{app\text{-}conv}$ (which is the convergent value of $D_{app}$) decreased by approximately 2.8% from that obtained when fitting to $c_{Bi} = c_1(x, t)$. The systematic error of 2.8% owing to averaging effect was eliminated by fitting the corrected analytical solution, as well as the $D_{app}$ value

obtained from the expected concentration, whose systematic error was 2.7%. However, the overestimation of the apparent diffusion coefficient remained for a short diffusion time, although averaging effect was eliminated.

### 5.2. Correction for initial mass transport

Initial mass transport was evaluated with the $\Delta t$ value, which can be interpreted as the prolonged diffusion time with the actual time origin earlier than the set one. **Figure 7** shows the fitted $c_{Bi} = c_2(x, t+\Delta t)$ in the entire time range with the variables of $\Delta t$ and $D$. The $\Delta t$ values in the fitted $c_{Bi} = c_2(x, t+\Delta t)$ in **Figs. 7(a)** and **(b)** were obtained as 265 s and 230 s, respectively. By fitting $c_{Bi} = c_2(x, t+\Delta t)$, according to **Fig. 10**, the overestimation of $D_{app}$ was reduced, and $D_{app\text{-}conv}$ was approximated as 4% less than that obtained by fitting $c_{Bi} = c_2(x, t)$.

The validity of the $\Delta t$ value obtained by fitting $c_{Bi} = c_2(x, t+\Delta t)$ was evaluated by calculating the additional mean square displacement (MSD) caused by initial mass transport. The additional MSD was estimated from the actual length of the solidified Sn-Bi rod described in Subsection 4.4. A quadratic function was fitted to the rod shape, as shown in **Fig. 8(a)**. The actual length of the Sn-Bi rod was calculated by averaging the volumes of the fitted shapes. The actual length $L'$ was estimated to be 3.35 mm. When $L'$ was larger than the planned length $L$, the additional MSD in the diffusion couple was caused by a variation in the initial concentration distribution, as described in **Fig. 8(b)**. The MSD in the capillary can be expressed as $L^2 / 3$ when the concentration varies from $c_{Bi} = \delta(x)$ to the set initial concentration condition, which is expressed as $c_{Bi} = c_0$ at $0 < x < L$ mm and $c_{Bi} = 0$ at $x > L$ mm. Hence, when the length of the Sn-Bi rod varies from $L$ to $L'$, the variation in the MSD in the capillary is expressed as $(L'^2 - L^2) / 3$. With the above calculation, the additional MSD was estimated to be $7.5 \times 10^{-7}$ m$^2$ when $L' = 3.35$ mm. According to Subsection 4.4, the maximum length of the solidified Sn-Bi rod was 3.48 mm. If the value is less than 3.48 mm, the additional MSD would be less than $1.03 \times 10^{-6}$ m$^2$. However, the additional MSD also increases from the above value by the mixing the rods in the initial state. The MSD caused by the initial mass transport was estimated to be (1.25 or 1.10) $\times 10^{-6}$ m$^2$ as $2D\Delta t$. Here, the $D$ value was adopted as the $D_{app}$ value obtained by fitting, and $\Delta t$ was adopted as 265 s or 230 s, respectively. Therefore, the MSD caused by the initial mass transport in the present measurement was estimated to be $10^{-6}$ m$^2$. Furthermore, the $\Delta t$ value obtained by fitting $c_{Bi} = c_2(x, t+\Delta t)$ was valid to be the diffusion time prolonged by initial mass transport.

### 5.3. Verification of matrix effect

**Figure 6(b)** shows the fitted linear and quadratic functions for all the detected intensities. The R-square values of both the functions were larger than 0.999 and equivalent. This indicated that no significant error was caused by matrix effect in the concentration measurement, where the Bi concentration was in the range of 0-2 at.%. When the initial Bi concentrations of the Sn-Bi rod were 5 and 10 at.%, the measured Bi concentrations at the measurement point ranged from 0 to 0.8 at.% and from 0 to 1.5 at.%, respectively. As shown in **Fig. 10**, the relative difference between the $D_{app\text{-}conv}$ values in the two concentration ranges was 1.6% in the results obtained after eliminating the averaging effect and initial mass transport. The uncertainty of the measured diffusion coefficient by using in-situ XRF was reported to be ±4% in the reference[21]. This is larger than the relative difference of the measured values in the present study. Therefore, matrix effect was also negligible in the diffusion measurements, according to the calibration curve and the two measured diffusion coefficients in different concentration ranges.

### 5.4. Validity of the apparent diffusion coefficient

The apparent diffusion coefficient became more statistically reliable and closer to the true diffusion coefficient with the increase in diffusion time[21]. The convergent values of the apparent diffusion coefficients $D_{app\text{-}conv}$ were $2.36 \times 10^{-9}$ m$^2$/s and $2.40 \times 10^{-9}$ m$^2$/s when the initial Bi concentrations of the Sn-Bi rods were 5 at.% and 10 at.%, respectively. The impurity diffusion coefficients of Bi in liquid Sn at 573 K were reported as $2.4 \times 10^{-9}$ m$^2$/s[13,22]. These were measured through the SC on the ground. The measured value in space was also reported with the estimated uncertainty as $(2.4 \pm 0.24) \times 10^{-9}$ m$^2$/s [8]. The $D_{app\text{-}conv}$ values obtained in the present study agree with the previously measured values. In the present study, the overestimation of the apparent diffusion coefficient was reduced, and the convergent apparent diffusion coefficient was decreased by eliminating averaging effect and initial mass transport. As a result, 2.8% and 4% of the systematic errors owing

to averaging effect and initial mass transport, respectively, were eliminated from the measured diffusion coefficients, and the $D_{app\text{-}conv}$ value agreed with the previously measured values.

Natural convection was determined to be suppressed sufficiently by adopting stable density layering[4] in the diffusion couple. The impurity diffusion coefficient was measured accurately using stable density layering in the reference[13,22]. The present measured diffusion coefficients ($2.36 \times 10^{-9}$ m$^2$/s and $2.40 \times 10^{-9}$ m$^2$/s) do not differ significantly from the reference value ($(2.4 \pm 0.24) \times 10^{-9}$ m$^2$/s). Therefore, the present values have no significant errors owing to natural convection. The concentration dependence of the diffusion coefficient of Bi in Sn was reported to be negligible in the Bi concentration range of 1-5 at.%[22]. Although the Bi concentration range was up to 10 at.% in the present study, the measured diffusion coefficients in different concentration ranges were not significantly different owing to concentration dependence. According to **Fig. 10**, a maximum overestimation of +6% in the $D_{app}$ value still occurred at a short diffusion time although the error factors were eliminated. The $D_{app\text{-}conv}$ value was not significantly different from the previously measured value. Therefore, the above overestimation was assumed to be caused by statistical uncertainty.

## 6. Conclusions

This study aimed to quantitatively evaluate and eliminate the dominant error factors in diffusion measurements using in-situ XRF. The diffusion coefficient of Bi in liquid Sn at 573 K was measured using in-situ XRF and LC. Matrix effect was demonstrated to induce no significant error in the measured diffusion coefficient by verifying the linearity of the calibration curve and comparing the measured diffusion coefficients under different concentration conditions. A systematic error in the apparent diffusion coefficient is caused by averaging effect and initial mass transport. The aforementioned error factors can be eliminated as follows:

- Averaging effect can be eliminated by convoluting the analytical solution of the actual concentration variation with the distribution of the X-ray fluorescence intensity scanned from the capillary. The systematic error in the present measurements eliminated by the above correction was equivalent to that in the simulation of the diffusion measurement analysis.
- Initial mass transport can be eliminated by shifting the point of time origin to a latter time point in the diffusion measurement by fitting the measured concentration variation. The amount of shift at the point of time origin was validated by calculating the additional mean square displacement from the shape of the diffusion couple at the initial state.


## Acknowledgments

This study was supported by the Japan Aerospace Exploration Agency (JAXA) Working group on "Diffusion Phenomena in Melts", Grant-in-Aid for Mitsubishi Materials Corporation in the fiscal year 2021, Grant-in-Aid for Scientific Research(C) Grant Number JP19K04990, Grant-in-Aid for JSPS Research Grant Number JP20J14950, Grant-in-Aid for JST SPRING Grant Number JPMJS2128, and Grant-in-Aid for Young Scientists (Early Bird) in Waseda Research Institute for Science and Engineering. We thank Kimura Foundry Co., Ltd. and the Kagami Memorial Research Institute for Materials Science and Technology for their financial support.


## Conflicts of Interest

The authors declare no conflict of interest.

## Nomenclature

| | |
|---|---|
| $c_0$ | Initial Bi concentration of the Sn-Bi rod (at.%) |
| $c_1(x, t)$ | Analytical solution of Fick's second law (at.%) |
| $c_2(x, t)$ | Corrected analytical solution of Fick's second law (at.%) |
| $c_{Bi}$ | Bi concentration (at.%) |
| $D$ | Diffusion coefficient (m$^2$/s) |
| $D_{app}$ | Apparent diffusion coefficient (m$^2$/s) |
| $D_{app\text{-}conv}$ | Convergent value of apparent diffusion coefficient (m$^2$/s) |
| $I$ | X-ray fluorescence intensity (cps) |

| | |
|---|---|
| $I_0$ | Total detected intensities in the capillary (cps) |
| $L$ | Planned length of the Sn-Bi rod at the initial state (mm) |
| $L'$ | Actual length of the Sn-Bi rod at the initial state (mm) |
| $t$ | Measurement time (s) |
| $\Delta t$ | Difference from the set time origin point to the actual one (s) |
| $u$ | Position in the capillary (mm) |
| $x$ | Position of the center of the X-ray irradiation range (mm) |
| $x_b$ | Position of the boundary between the dummy and sample (mm) |
| $\Delta x$ | Distance from the center of the X-ray irradiation range to the detected point (mm) |
| $\rho_I(x\text{-}u)$ | Intensity scanned from a position $u$ in the capillary when the position of the center of the irradiated range is $x$. (cps) |
| $\sigma$ | Standard deviation of the Gaussian function in a width direction (mm) |

## References


1) H. Müller and G. Müller-Vogt: Investigation of additional convective transports in liquid metals and semiconductors during diffusion measurements by means of the shear cell technique. Cryst. Res. Technol., **38** (2003) 707, DOI: 10.1002/crat.200310085.
2) R. Roşu-Pflumm, W. Wendl, G. Müller-Vogt, S. Suzuki, K.-H. Kraatz and G. Frohberg: Diffusion measurements using the shear cell technique: Investigation of the role of Marangoni convection by pre-flight experiments on the ground and during the Foton M2 mission. Int. J. Heat Mass Transf., **52** (2009) 6042, DOI: 10.1016/j.ijheatmasstransfer.2009.06.001.
3) V. Botton, P. Lehmann, R. Bolcato, R. Moreau and R. Haettel: Measurement of solute diffusivities. Part II. Experimental measurements in a convection-controlled shear cell. Interest of a uniform magnetic field. Int. J. Heat Mass Transf., **44** (2001) 3345, DOI: 10.1016/S0017-9310(00)00362-8.
4) S. Suzuki, K.-H. Kraatz and G. Frohberg: Diffusion experiments in liquid Sn-Bi and Al-Ni systems with a stable density layering using the FOTON shear cell under 1g conditions. Microgravity Sci. Technol., **16** (2005) 120, DOI: 10.1007/BF02945961.
5) F. Onishi, T. Miyake, Y. Inatomi and K. Kuribayashi: Measurements of interdiffusion coefficients in metallic melts at high temperature under horizontal static magnetic field. Microgravity Sci. Technol., **18** (2006) 86, DOI: 10.1007/BF02870386.
6) Y. Liu, W. Lin, B. Zhou, T. Zheng, Y. Zhong and L. Zhang: A novel gravity-assisted automatic docking device for studying diffusion in liquid metal melts assisted by a strong static magnetic field. Rev. Sci. Instrum., **92** (2021) 094903, DOI: 10.1063/5.0063320.
7) G. Mathiak, A. Griesche, K.-H. Kraatz and G. Frohberg: Diffusion in liquid metals. J. Non-Cryst. Solids, **205–207** (1996) 412, DOI: 10.1016/S0022-3093(96)00253-0.
8) J.P. Garandet, G. Mathiak, V. Botton, P. Lehmann and A. Griesche: Reference Microgravity Measurements of Liquid Phase Solute Diffusivities in Tin- and Aluminum-Based Alloys. Int. J. Thermophys., **25** (2004) 249, DOI: 10.1023/B:IJOT.0000022338.21866.f9.
9) A. Griesche, K.-H. Kraatz and G. Frohberg: A modified shear cell for mass transport measurements in melts. Rev. Sci. Instrum., **69** (1998) 315, DOI: 10.1063/1.1148516.
10) S. Suzuki, K.-H. Kraatz and G. Frohberg: Ground-based diffusion experiments on liquid Sn-In systems using the shear cell technique of the satellite mission Foton-M1. Ann. N. Y. Acad. Sci., **1027** (2004) 169, DOI: 10.1196/annals.1324.016.
11) T. Masaki, T. Fukazawa, S. Matsumoto, T. Itami and S. Yoda: Measurements of diffusion coefficients of metallic melt under microgravity - Current status of the development of shear cell technique towards JEM on ISS. Meas. Sci. Technol., **16** (2005) 327, DOI: 10.1088/0957-0233/16/2/002.
12) Y. Geng, C. Zhu and B. Zhang: A sliding cell technique for diffusion measurements in liquid metals. AIP Adv., **4** (2014) 037102, DOI: 10.1063/1.4868382.
13) S. Suzuki, K.H. Kraatz and G. Frohberg: The effect of shear convection on diffusion measurements in liquid metals using the Foton shear cell. Microgravity Sci. Technol., **18** (2006) 155, DOI: 10.1007/BF02870400.
14) B. Zhang, A. Griesche and A. Meyer: Diffusion in Al-Cu Melts Studied by Time-Resolved X-Ray Radiography. Phys. Rev. Lett., **104** (2010) 035902, DOI: 10.1103/PhysRevLett.104.035902.

15) C. Neumann, E. Sondermann, F. Kargl and A. Meyer: Compact high-temperature shear-cell furnace for in-situ diffusion measurements. J. Phys. Conf. Ser., **327** (2011) 012052, DOI: 10.1088/1742-6596/327/1/012052.
16) A. Griesche, B. Zhang, E. Solórzano and F. Garcia-Moreno: Note: X-ray radiography for measuring chemical diffusion in metallic melts. Rev. Sci. Instrum., **81** (2010) 056104, DOI: 10.1063/1.3427256.
17) T. Schiller, E. Sondermann and A. Meyer: New Analyzing Approaches for In Situ Interdiffusion Experiments to Determine Concentration-Dependent Diffusion Coefficients in Liquid Al–Au. Metals, **11** (2021) 1772, DOI: 10.3390/met11111772.
18) T. Ujihara, K. Fujiwara, G. Sazaki, N. Usami and K. Nakajima: New method for measurement of interdiffusion coefficient in high temperature solutions based on Fick's first law. J. Cryst. Growth, **241** (2002) 387, DOI: 10.1016/S0022-0248(02)01316-7.
19) T. Masaki and S. Suzuki: Measurement of Diffusion Coefficients in Melts by Using an X-ray Fluorescence. Sp. Utili. Res., **29** (2015) 103.
20) K. Fujita, Y. Shimura, S. Suzuki and T. Masaki: Feasibility Study of in-situ Observation of Diffusion in Liquid Metals by using a Fluorescent X-ray Spectroscopy. Int. J. Microgravity Sci. Appl., **35** (2018) 350404, DOI: 10.15011/jasma.35.4.350404.
21) Y. Kobayashi, M. Shiinoki, R. Yamatake, T. Masaki and S. Suzuki: Required Diffusion Time for in-situ Measurement of Diffusion Coefficients in Liquid Alloys by X-ray Fluorescence Analysis. Int. J. Microgravity Sci. Appl., **38** (2021) 380302, DOI: 10.15011/jasma.38.380302.
22) M. Shiinoki, N. Hashimoto, H. Fukuda, Y. Ando and S. Suzuki: Self-diffusion Measurements of Liquid Sn Using the Shear Cell Technique and Stable Density Layering. Metall. Mater. Trans. B, **49** (2018) 3357, DOI: 10.1007/s11663-018-1416-3.
23) T. Arai: 1.4.1 Correction of Matrix Element Effects. In Handbook of Practical X-Ray Fluorescence Analysis, Springer (2005).
24) E. Gillam and H.T. Heai: Some problems in the analysis of steels by X-ray fluorescence. Br. J. Appl. Phys., **3** (1952) 353, DOI: 10.1088/0508-3443/3/11/304.
25) T. Shiraiwa and N. Fujino: Theoretical Calculation of Fluorescent X-Ray Intensities in Fluorescent X-Ray Spectrochemical Analysis. Jpn. J. Appl. Phys., **5** (1966) 886, DOI: 10.1143/JJAP.5.886.
26) R. Klockenkämper and A. von Bohlen: Determination of the critical thickness and the sensitivity for thin-film analysis by total reflection X-ray fluorescence spectrometry. Spectrochim. Acta Part B At. Spectrosc., **44** (1989) 461, DOI: 10.1016/0584-8547(89)80051-5.
27) R.M. Rousseau: Concept of the Influence Coefficient. Rigaku Journal, **18** (2001) 8, DOI: 10.12691/jgg-1-1-1.
28) J. Karjou: Matrix effect on the detection limit and accuracy in total reflection X-ray fluorescence analysis of trace elements in environmental and biological samples. Spectrochim. Acta Part B At. Spectrosc., **62** (2007) 177, DOI: 10.1016/j.sab.2007.02.003.
29) A. von Bohlen and R. Fernández-Ruiz: Experimental evidence of matrix effects in total-reflection X-ray fluorescence analysis: Coke case. Talanta, **209** (2020) 120562, DOI: 10.1016/j.talanta.2019.120562.
30) R. Yamatake, M. Shiinoki, Y. Kobayashi, T. Masaki and S. Suzuki: Spectral Processing and Intensity Ratio Measurement Using X-ray Fluorescence Analysis in Liquid Alloys. Int. J. Microgravity Sci. Appl., **38** (2021) 380303, DOI: 10.15011/jasma.38.380303.
31) M. Shiinoki, Y. Ando, H. Fukuda, S. Suzuki and T. Masaki: Effects of Container Materials on X-ray Fluorescence Spactra and Detection Time for *In-situ* X-ray Fluorescence Composition Analysis of Liquid Metals. Int. J. Microgravity Sci. Appl., **35** (2018) 350403, DOI: 10.15011//jasma.35.350403.
32) H. Okashita: Primary Beam Filter Method for Fluorescent X-ray Analysis. Adv. X-Ray Chem. Anal., Jpn 8 (1976) 105.
33) A.C. Thompson and D. Vaughan: Table 1-2. Photon energies, in electron volts, of principal K-, L-, and M-shell emission lines. In X-Ray Data Booklet, 3rd ed., Lawrence Berkeley National Laboratory (2009).
34) W.F. Gale and T.C. Totemeier: Smithells Metals Reference Book, 8th ed., Elsevier Butterworth-Heinemann (2004).